

PAPER

# Tunable electromagnetic shunt damper with opposing magnets configuration

To cite this article: Ruqi Sun *et al* 2020 *Smart Mater. Struct.* **29** 115034

View the [article online](#) for updates and enhancements.

# Tunable electromagnetic shunt damper with opposing magnets configuration

Ruqi Sun , Waion Wong  and Li Cheng 

Department of Mechanical Engineering, The Hong Kong Polytechnic University, Hong Kong, People's Republic of China

E-mail: [ruqi.sun@connect.polyu.hk](mailto:ruqi.sun@connect.polyu.hk)

Received 1 May 2020, revised 28 July 2020

Accepted for publication 24 August 2020

Published 2 October 2020



CrossMark

## Abstract

Electromagnetic damper (EMD) has been widely studied in the control of vibrating structures. It has higher tunability when compared with a viscous damper and lower cost when compared with a magnetorheological damper. However, its use is limited mainly due to the high ratios of system mass/volume to the damping force produced. In this paper, an electromagnetic shunt damper (EMSD) with opposing magnets configuration to provide a tunable damping force is proposed for vibration damping applications. The proposed EMSD configuration allows a significant reduction in size in comparison with other similar designs of EMSD found in the literature. Both simulations and experiments are conducted to verify the improvements of this proposed design over existing ones. In particular, an EMSD comprising six opposing magnets is designed and tested on a single-degree-of-freedom (SDOF) vibration system. The damping coefficient of the proposed EMSD offers a large tunable range with maximum damping coefficient about nine times or 900% of the minimum damping coefficient. As a result, the force and displacement transmissibilities can be minimized in a wide frequency band by varying the damping ratio in the SDOF system at different vibrating frequencies.

Keywords: tunable electromagnetic shunt damper, opposing magnets configuration, vibration isolation, tunable damping

(Some figures may appear in colour only in the online journal)

## 1. Introduction

A vibration damper is an important device for suppressing machine vibrations. Tunable damping can help maximize the effectiveness of the damper for vibration control under different working conditions. However, the damping coefficient of viscous dampers is fixed once it is manufactured. On the other hand, magnetorheological dampers usually incur high cost, thus hampering their widespread use. An electromagnetic shunt damper (EMSD) was first designed by Sam [1] to provide damping force to mechanical systems. Then, EMSDs were widely used as a vibration damper or an energy harvester. As a useful analysis metric, the electromechanical coupling coefficient was deduced when an EMSD was used as a vibration damper or an energy harvester [2]. EMSDs were utilized for vibration isolation in different kinds of beams and plates for their high tunability by varying the impedance of the

shunt circuit [3, 4]. Connected with a resonant shunt circuit, it was also be used for vibration control in civil engineering [5]. Other applications of EMSDs include micro-vibration isolation by connecting to a negative resistance circuit [6] and for energy harvesting in a vehicle vibration isolation system [7]. More specifically, Stabile [8] proposed an opposing magnets configuration with iron yoke spacers in between the magnets, and Zuo [9] proposed a similar configuration with 1018 steel spacers. The opposing magnets configuration showed some improvement in terms of vibration suppression [9] and energy harvesting [10].

Negative resistance can improve the damping force range of an EMSD. However, its implementation demands additional energy supply devices. Moreover, researches on alternative EMSD designs and configurations are scarce since the original idea was first proposed. This forms the major motivation behind the present research.

In this paper, a tunable EMSD with tightly connected opposing magnets configuration is proposed, designed and tested by both simulations and experiments. The transduction factors of the proposed design is compared to those of [9] and [10]. Furthermore, the vibration isolation effectiveness of the proposed design is demonstrated by applying the proposed EMSD as a tunable damper in a SDOF vibration system. The proposed EMSD can be applied to minimize the vibration transmissibility of the vibrating system by varying the damping force at different vibrating frequencies.

## 2. Design and model analysis of EMSD

### 2.1. Overview of electromagnetic shunt damper

A simple configuration of electromagnetic shunt damper (EMSD) contains one magnet and one coil which is connected to an outer circuit as shown in figure 1(a). The Lorentz force generated in the EMSD when relative motion occurs between the magnet and the inductor of the circuit can be used as a damping force for vibration control. A variable resistor is connected to the coil as shown in figure 1(b) for the adjustment of the current in the circuit. The coil is represented by connecting an electromotive force (EMF), a resistor and an inductor in series as shown in figure 1(b). Since the inductance is only several milli-Henry and the EMSD is designed to be used at the frequency domain lower than 30 Hz, the impedance contributed from the coil inductance is ignored.

### 2.2. Basic concepts and working principle of the EMSD

EMSD may be regarded as a linear power generator which converts mechanical power into electrical power and dissipates thermal energy as waste in the conversion process.

According to the Faraday-Lenz law, the electromotive force (EMF)  $\varepsilon$  is the induced voltage of EMSD generated when a conductor of length  $l$  (m) moves in a constant magnetic field of strength  $B$  (T) at a constant velocity  $v$  ( $\text{m s}^{-1}$ ). The EMF can be expressed as

$$\varepsilon = Blv \quad (1)$$

A simplified analysis is conducted to obtain the transduction efficiency of the electromagnetic shunt damper by considering a single loop of the coil, shown in figure 1(a). Since the relative motion occurs in the  $x$ -direction and only the magnetic flux passing through the conductor circuit will contribute to the EMF, the vertical magnetic flux density  $B_x$  makes no contribution to the EMF. Therefore, the radial magnetic flux density  $B_r$  is the only activator for the induced EMF. The EMSD induced voltage  $\varepsilon$  can be written as

$$\varepsilon = - \oint_{loop} B_r(x, r) dl \dot{x} \quad (2)$$

The transduction factor  $K_t$ , which represents the transduction efficiency of the conversion from mechanical energy to

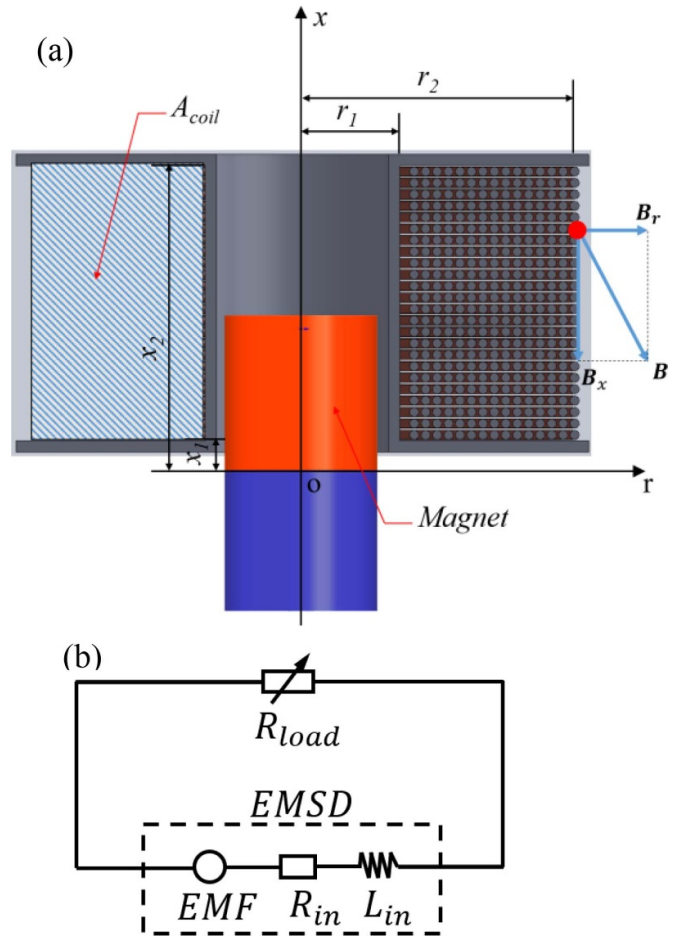


**Figure 1.** Structure configuration of electromagnetic shunt damper: (a) the magnet and the coil, (b) the equivalent circuit of the coil and its connected resistor.

electrical energy, can be defined as

$$K_t = - \oint_{loop} B_r(x, r) dl \quad (3)$$

Moreover, by extending the single loop coil to the whole coil as shown in figure 1(a), the transduction factor can be expressed as [11]

$$K_t = - \frac{l_{wire}}{A_{coil}} \int_{r_1}^{r_2} \int_{x_1}^{x_2} B_r(x, r) dx dr \quad (4)$$

where  $l_{wire}$  denotes the length of the whole coil and  $A_{coil}$  its cross-sectional area as shown in figure 1(a). Using equations (2) and (3), we can write

$$\varepsilon = K_t \dot{x} \quad (5)$$

If the coil is connected with a variable resistor in the circuit as shown in figure 1(b), the current  $i$  will be generated and the Lorentz force is exerted on the coil to hinder the movement of the magnet. The reaction force may be called the equivalent damping force  $F_e$ . The current can be obtained based on the Kirchhoff circuit law and the total circuit impedance  $Z$ ,

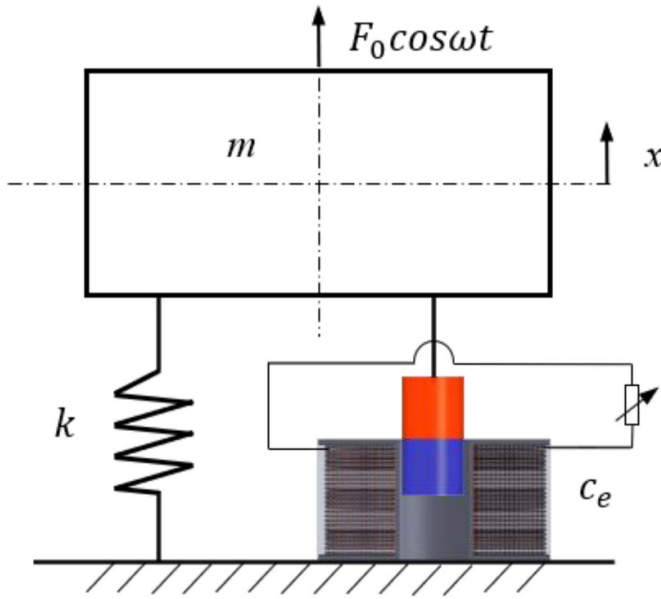


**Figure 2.** Single degree of freedom vibration system with electromagnetic shunt damper.

which includes the coil resistance  $R_{in}$ , coil inductance  $L_{in}$  and the external resistance  $R_{load}$ .

$$F_e = K_t i = \frac{K_t \varepsilon}{Z} \quad (6)$$

Using equation (5) and equation (6), the equivalent damping force may be written as

$$F_e = \frac{K_t^2}{Z} \dot{x} \quad (7)$$

Based on the damping force definition, the damping coefficient  $c_e$  can be expressed as

$$c_e = \frac{K_t^2}{Z} \quad (8)$$

When the EMSD is applied in a SDOF vibration system as shown in figure 2, the equation of motion can be expressed as

$$m\ddot{x} + c_e \dot{x} + kx = F_0 \cos \omega t \quad (9)$$

where  $k$  denotes the stiffness;  $m$  is the mass and  $x$  is the vertical displacement. The force transmissibility from the vibrating mass to the base can be derived and written as

$$T_f = \sqrt{\frac{1 + (2\zeta\gamma)^2}{(1 - \gamma^2)^2 + (2\zeta\gamma)^2}} \quad (10)$$

where  $\gamma = \omega/\omega_n$  is the frequency ratio between the excitation frequency and the natural frequency of the SDOF system.  $\zeta = c_e/(2\sqrt{km})$  is the damping ratio. The variation of the force transmissibility with the frequency ratio and damping ratio is shown in figure 3.

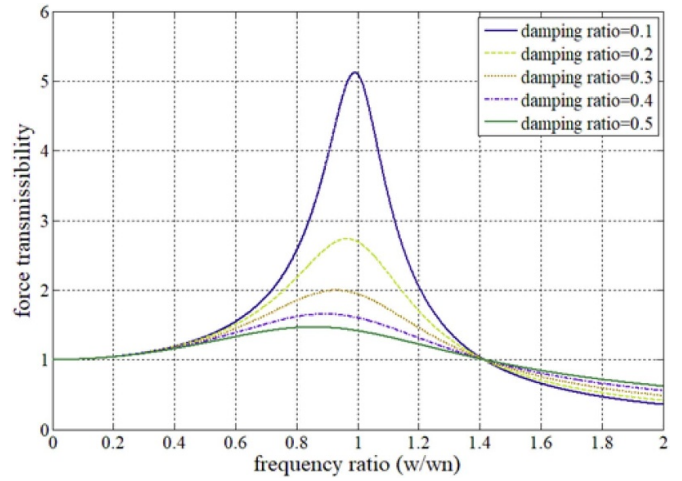


**Figure 3.** Variation of force transmissibility with frequency ratio and damping ratio.

The force transmissibility can be minimized if different damping ratios could be achieved in different frequency domains. While a higher damping ratio is necessary to contain the system resonance in the low-frequency range of  $\gamma < \sqrt{2}$ , a lower damping ratio ensures better isolation effect in the higher frequency range of  $\gamma > \sqrt{2}$ . As shown in figure 3, all the transmissibility curves intersect at a point of frequency ratio  $\gamma = \sqrt{2}$ . This intersection point is denoted as IP in the following sections. The tunable damping function of the proposed EMSD can help minimize the transmissibility of the SDOF system in the whole frequency domain by adjusting the damping force in different vibrating frequency ranges.

### 2.3. Opposing magnets configuration

The EMSD performance can be enhanced by using different magnet configurations to improve the radial magnetic flux density distribution. Different configurations of magnets have been proposed [9, 10] to achieve greater transduction efficiency. It is shown in the following section the proposed magnet configuration without spacer is better than the magnet configuration with spacer [9, 10] in terms of transduction efficiency. The transduction factor of the two designs of magnet configurations, one without spacer and the other with an iron yoke spacer, are compared by simulation in the following section.

**2.3.1. Magnetic flux density simulation.** The two opposing magnets are N32 NdFeB ring-shaped permanent magnets with 4 mm inner diameter (the hole is shown by the dash line in figure 4(a)), 14 mm external diameter and 10 mm thickness as shown in figure 4(a). The two magnets are aligned in opposite polarity such that the two S magnetic poles are physically connected. The magnetic flux density distribution around the magnets was simulated with the free magnetic analysis software FEMM. As shown in figure 4(b), the magnetic flux densities around the S magnetic pole of the cylindrical side surface are greatly increased when compared to that of the N magnetic

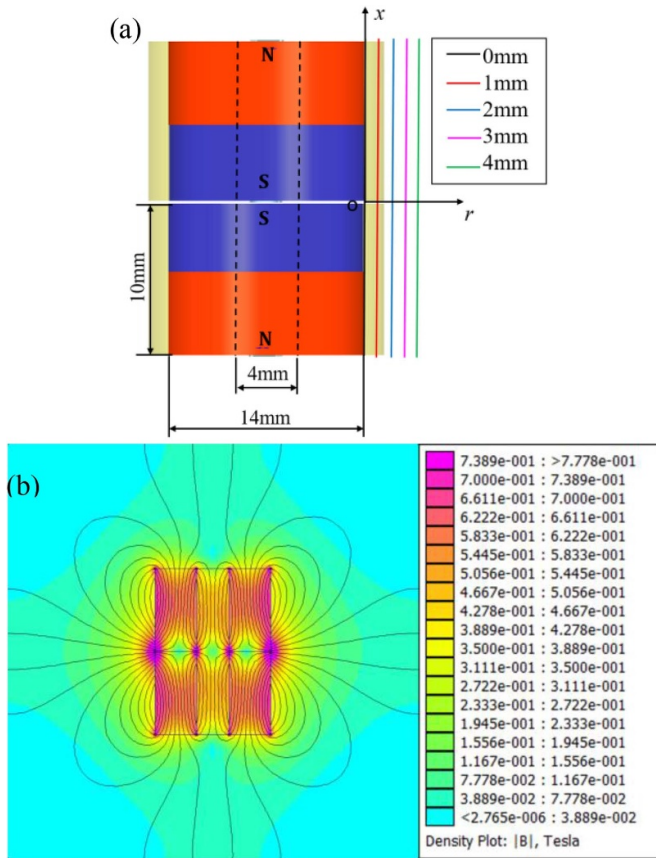


**Figure 4.** Two-opposing-magnets permutation: (a) the schematic and dimensions, (b) simulation results of magnetic flux density.

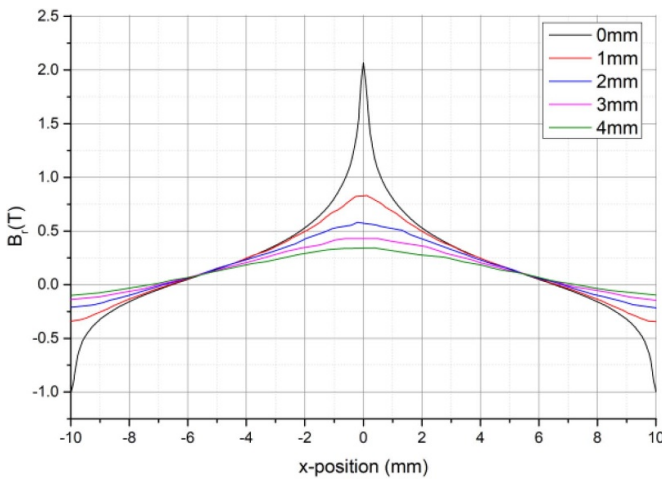


**Figure 5.** Variation of radial magnetic flux density ( $B_r$ ) along the lines of 0 mm, 1 mm, 2 mm, 3 mm, 4 mm in figure 4(a).

poles. In order to demonstrate the enhanced value of radial magnetic flux density, the variation in the radial magnetic flux density  $B_r$  along the five straight line segments each of 20 mm long in figure 4(a) is plotted in figure 5 for illustration.

Since the  $N$  magnetic poles are far away from the connecting surfaces of the two magnets, the magnetic lines around the  $N$  poles remain almost the same after the connection. The

**Table 1.** Transduction factors of the three magnet configurations.

Magnet Con-figuration	One magnet	Two homodromous magnets	Two opposing magnets
Transduction factor $K_t$	0.001	0.0011	3.4435

radial magnetic flux density at the  $N$  magnetic pole is therefore used as the datum flux density for comparison of the flux densities at different locations around the magnet pair. Take the 0 mm curve as an example, the radial magnetic flux density,  $B_r$ , is about 2.1 Tesla at  $x = 0$  mm. However,  $B_r$  is just about 1 Tesla at  $x = \pm 10$  mm. Therefore, the maximum radial magnetic flux density,  $B_r$ , is increased by more than 100% by using the proposed opposing magnets configuration. Moreover, the other four curves also show similar variation trends. However, the maximum radial magnetic flux density decreases sharply with the distance between the radial position and cylindrical side surface. Therefore, the coil should be as close as possible to the cylindrical surface of the magnet pair if a larger Lorentz force needs to be induced when the magnets are moving along the  $x$ -axis. As a result, the maximum radial magnetic flux density can be greatly increased with the proposed design of EMSD.

**2.3.2. Transduction factor identification.** The transduction factor,  $K_t$ , which denotes the energy transfer efficiency is considered in this section. The transduction factor is calculated by extracting the radial magnetic flux density data from FEMM and conducting the integration as expressed by equation (4). Three different magnet configurations: single magnet, two opposing magnets, and two homodromous magnets, as shown in figure 8(a) are compared. The inner diameter of the coil skeleton is 16 mm. With the skeleton measured 1 mm in thickness, the inner diameter of the coil is therefore 18 mm. The external diameter is 32 mm and the height is 20 mm. The cross-section area  $A_{coil}$  is therefore 7 mm  $\times$  20 mm, and the  $l_{wire}$  is about 40 m. Moreover, the parameters of magnets are the same as those in the previous section. The numerical results of the transduction factor of the three different magnet configurations are shown in table 1.

As shown in table 1, the EMSD with the proposed opposing magnets configuration offers a significant increase of the transduction factor. Experimental comparison of these three magnet configurations is shown in the next section.

In the following, the proposed EMSD is compared to the designs of Stabile [9] and Zuo [10] with respect to the magnetic flux density distribution and the transduction factor  $K_t$  by simulation. In the simulation, the combined length of the magnets and the spacer is assumed to be 20 mm. Since the ratio of magnet length to the spacer length adopted by Zuo [10] is 6.35 mm to 5 mm, the corresponding ratio in this simulation model is set as 7 mm to 6 mm as shown in figure 6. The grey block in figure 6 represents the spacer. The material of the spacer is carpenter silicon core iron 'A' in Stabile's design [9] and 1018 steel in Zuo's design [10].

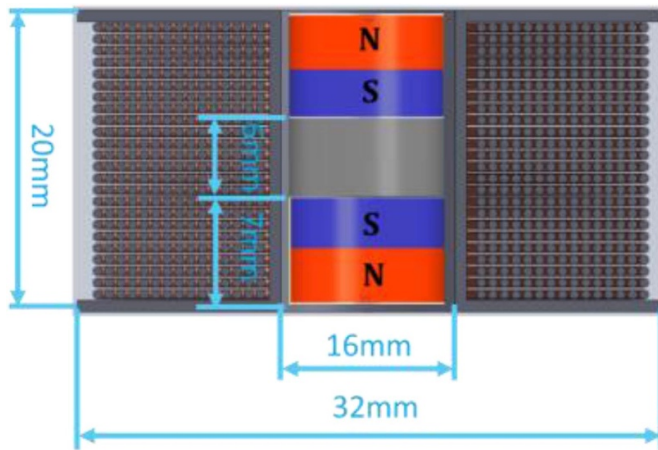


**Figure 6.** Structure and dimensions of the opposing magnets configuration with spacer in between the magnets.

**Table 2.** Transduction factors of EMSD of three different opposing magnets configuration.

Opposing magnets configurations	Iron yoke spacer [9]	1018 steel spacer [10]	Present design
Transduction factor $K_t$	3.4056	3.4050	3.4435

The magnetic flux density distribution and the transduction factor  $K_t$  of the EMSD of two configurations using different materials are shown in figure 7 and table 2, respectively. As shown in figure 7, the magnetic flux density distributions are similar in the designs of [9] and [10] except a small difference of the maximum magnetic flux density.

As shown in table 2, the transduction factors derived for the designs of [9] and [10] are almost the same because the magnetic flux density distributions of these two designs are very similar. The total length of the magnet stack in the proposed design is 14 mm while those in the designs of [9] and [10] are 20 mm. Therefore, the proposed design has a size reduction of about  $6/20 = 30\%$ . While maintaining the same amount of energy transduction, the proposed design has a significant reduction in the size to damping force ratio in comparison to the designs of Stabile [9] and Zuo [10].

**2.3.3. Experimental verification of EMSD performance.** The damping characteristics of EMSD with the three magnet configurations as shown in figure 8(a) were measured experimentally and compared. Under the same sinusoidal excitation at 1 Hz, the hysteresis loop tests of the three magnets configurations are conducted by measuring the force and the displacement of the magnets with the coil fixed on a mounting. The hysteresis loop curve can then be obtained by setting the displacement as the independent variable and the force as the dependent variable.

As shown in the hysteresis loops of the three magnet configurations in figure 8(b), the configuration using two homodromous magnets shows no significant improvement over the one with just one magnet. However, the area encircled by the

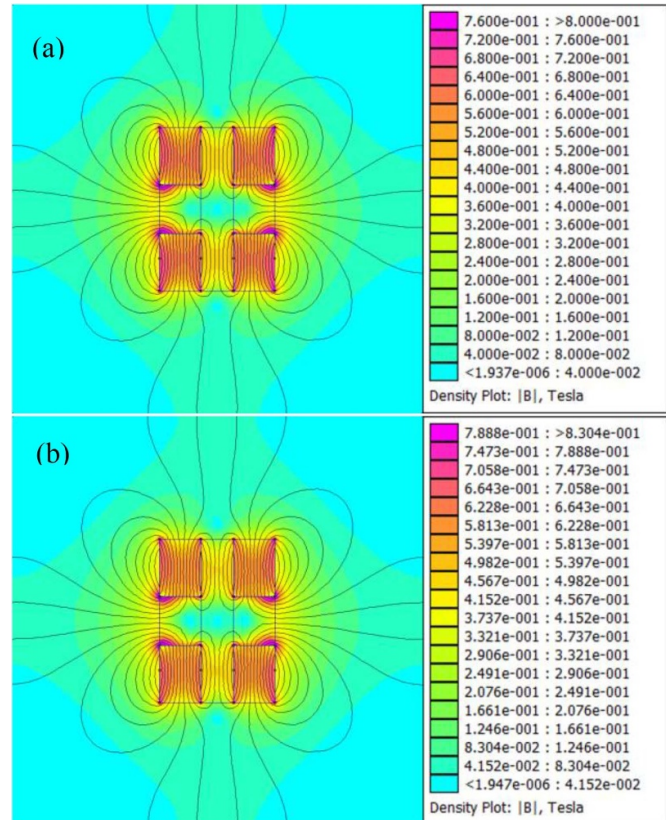


**Figure 7.** Simulation results of magnetic flux density of the two opposing magnets connected by: (a) 1018 steel, (b) carpenter silicon core iron 'A'.

hysteresis curve of the configuration with two opposing magnets is 200% larger than those of the other two configurations. Therefore, this experiment confirms that the proposed design of EMSD can absorb much more vibration energy than the other two cases.

Based on the magnetic flux density simulation, transduction factor estimation and experimental analysis of the hysteresis loop of the three different magnet configurations as shown in figure 8(a), the proposed two-opposing magnets configuration has been proved to be the best among the three magnet configurations. The damping performance of the proposed magnet configuration can be multiplied by expanding this kind of magnet configuration in series.

**2.3.4. Multiple opposing magnets configuration.** To increase the damping force of the proposed EMSD, six magnets are connected together with opposite polarities facing each other as illustrated in figure 9(a). The total length of the magnet stack is 42 mm. If the designs of [7] and [9] are used instead, then the total length of the magnet stack becomes  $42 + 36 = 78$  mm. The additional length is a result of adding the spacers placed between each magnet pair. Therefore, the proposed design has a size reduction of about  $36/78 = 46.2\%$ .

The EMSD damping coefficient would increase linearly with the increase of the number of magnets in the damper. In the testing prototype as shown in figure 11, if too many

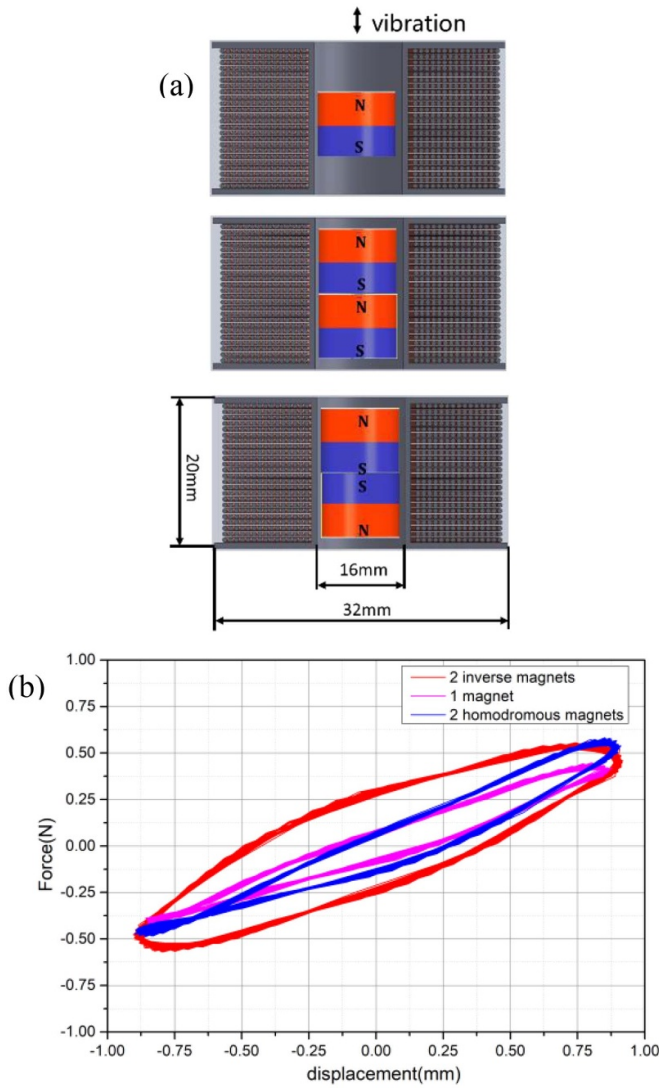


**Figure 8.** Three kinds of EMSD configuration: (a) the structure schematic, (b) the hysteresis loop of the EMSDs with 1 Hz sinusoidal vibration excitation.

magnet pairs are used, then the length of the SDOF vibrating system will become too long such that resonant vibration of the SDOF system may occur in the target excitation frequency range. For the SDOF system with the EMSD, measurement shows that its first resonant frequency is about 20 Hz with eight magnet pairs in the damper. The resonant frequency of the SDOF system increases when the number of magnet pairs in the damper decreases. Therefore, we used six opposing magnets pairs in the prototype so that the first resonant frequency of the vibration system is over 30 Hz which falls outside the range of the sweep sinusoidal excitation in the tests.

As shown in figure 9(b), the magnetic flux density peaks at positive value and negative value alternately. Each pair of the adjacent coils are connected at 180° phase angle by joining together their starting ends and their ending ends. The first and the last coils are connected to the external variable resistance as shown in figure 9(a). With resistance of each coil

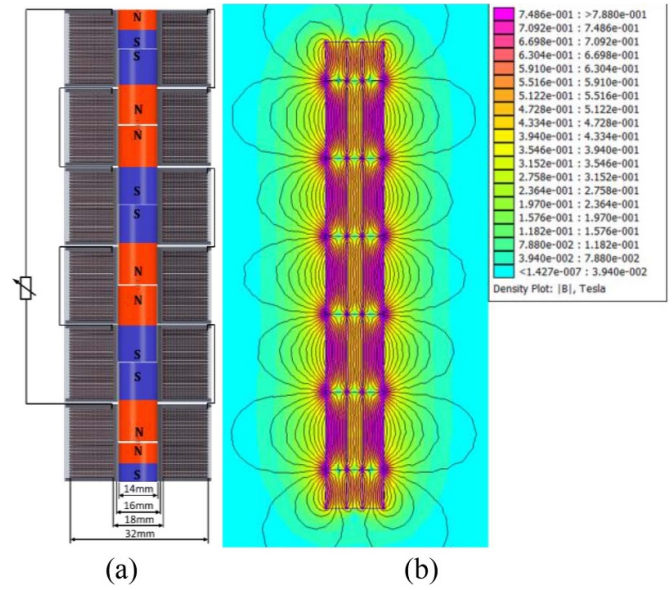


**Figure 9.** EMSD with multiple opposing magnets configuration: (a) the structure schematic, (b) magnetic flux density by simulation.

measures about 0.6 Ω, the total coil resistance in the circuit is about 3.6 Ω.

Simulation is also conducted to analyze the magnetic flux density of the six opposing magnets configuration, with results shown in figure 9(b). It can be seen that the corresponding magnetic flux density distributions are well proportioned of the two opposing magnets configuration simulated before. The magnetic induction lines in the middle region has a repeating pattern and they become sparsely distributed at both ends of the magnet stack.

### 3. Experimental test on the EMSD for vibration control

#### 3.1. SDOF vibration system with EMSD

The magnet stack comprising six opposing magnets are connected with a M4 screw through the central hole, and the six induction coils are connected with glues and fixed between the flanges of the casing as shown in figure 10(a). The electromagnetic shunt damper is assembled with the spring and mass to form a SDOF vibration system. By changing the mass and measuring the corresponding natural frequency variation, the stiffness and the actual mass of the SDOF system can be identified using equation (11) and equation (12) below.

$$m = k / (2\pi f_n)^2 \tag{11}$$

$$\Delta m = \left[ \frac{1}{(2\pi f_{n1})^2} - \frac{1}{(2\pi f_{n2})^2} \right] k \tag{12}$$

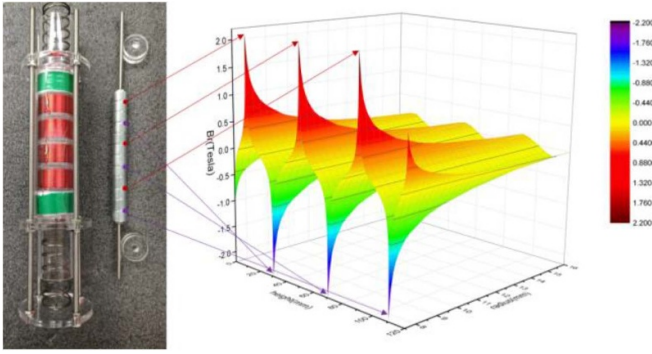


**Figure 10.** The six opposing magnets configuration: (a) the physical prototype (left), and (b) variation of the magnetic flux density with height and radius (right).

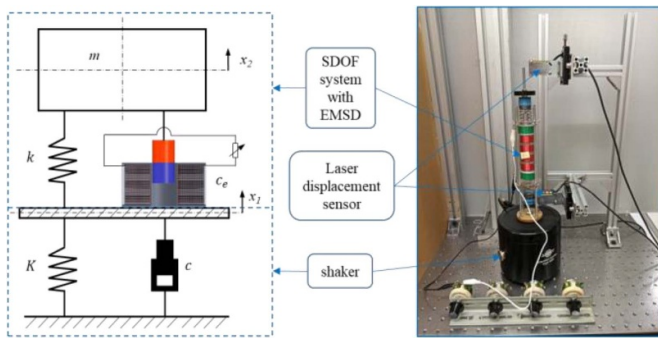


**Figure 11.** The experiment set up: schematic diagram (left) and test rig (right).

$\Delta m$  is the mass variation between the two measurements.  $f_{n1}$  is the natural frequency in angular unit with the first measurement.  $f_{n2}$  is the natural frequency in angular unit with the second measurement. Based on the three measurement results, the stiffness  $k$  is found to be  $1510.7 \text{ N m}^{-1}$ , and the effective mass is  $0.2936 \text{ kg}$ . The natural frequency of the SDOF system is tuned at  $11.422 \text{ Hz}$  by adjusting the mass of the system.

In theory, the displacement transmissibility of the SDOF system is the same as the force transmissibility. Since displacement is much easier to measure, which also offers greater accuracy than the force measurement, the displacement response is measured instead to illustrate both the displacement and force transmissibilities of the SDOF system.

The SDOF system as shown in figure 11 is connected to a shaker providing the swept sinusoidal excitation ( $0.01\text{--}30 \text{ Hz}$ ) at  $1.5 \text{ Hz s}^{-1}$ . The schematic diagram of the experimental setup is shown in the left diagram of figure 11. The system transmissibility is obtained by calculating the frequency response function (FRF) with the displacement signals  $x_1$  and  $x_2$ . Two Panasonic HG-C1030 laser displacement sensors are fixed on the support to measure the two displacements, and the measured signals are sent to B&K PULSE 7767 for analog to digital conversion. The frequency response function of this SDOF system can then be derived by the control computer with Fast Fourier Transform (FFT) algorithm.

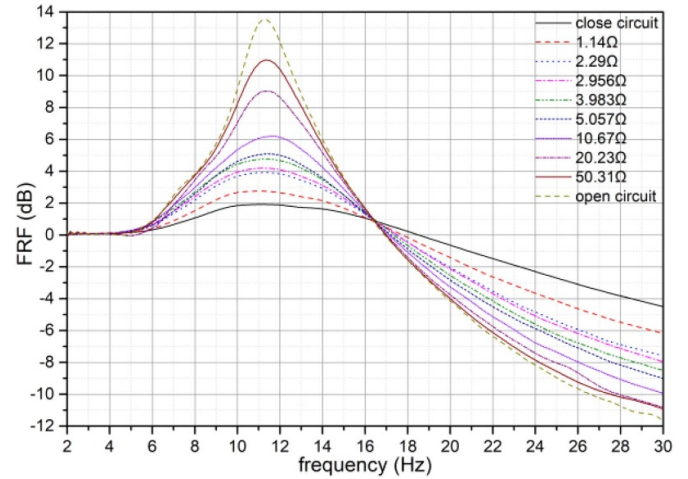


**Figure 12.** Frequency response function (FRF) of SDOF system with the EMSD external resistance variation.

### 3.2. Experimental analysis of tunable damping

Based on equation (8), the amount of damping that can be achieved using the proposed EMSD varies with the external resistance, which has been validated experimentally with the logarithmic decrement method [12]. Here, the displacement transmissibility of the SDOF system with different external resistance is measured and plotted in figure 12.

As shown in figure 12, the displacement transmissibility varies with the external resistance, and the variation matches the theoretical prediction as shown in figure 3. The intersection point at  $\gamma = \sqrt{2}$  of the transmissibility curve is located at  $16.5 \text{ Hz}$  which is about  $\sqrt{2}$  times of the natural frequency. This finding tallies with the theoretical prediction. To obtain the tunable damping range, the damping ratio is determined based on the half-power bandwidth method [13] as depicted by equation (13) below.

$$\zeta = \frac{1}{2} \frac{\Delta\omega}{\omega_n} \quad (13)$$

where  $\Delta\omega$  is the frequency bandwidth at which the transmissibility decreases by 3 dB from the maximum value. The damping coefficient can then be derived according to equation (14) below.

$$c_e = 2\zeta\sqrt{km} \quad (14)$$

The damping ratio and damping coefficient of the SDOF system are shown in table 3. The damping coefficient can be increased from about  $4 \text{ N s m}^{-1}$  to about  $40 \text{ N s m}^{-1}$  by increasing the external resistance from  $0 \text{ }\Omega$  to infinity at open circuit. Therefore, the damping coefficient of the proposed tunable damper offers a tunable range with maximum damping coefficient about nine times or 900% of its minimum damping coefficient. The corresponding damping ratio of the SDOF system varies between 0.0956 and 0.961. The curves of the damping coefficient of the damper with different external resistances are plotted in figure 13 to show its variations with the resistance.



**Table 3.** Damping coefficient of the damper and damping ratio of the SDOF system with different external resistances.

External resistance ( $\Omega$ )	Damping ratio	Damping coefficient ( $N \cdot s \cdot m^{-1}$ )
0 (close circuit)	0.961	40.463
1.14	0.424	17.862
2.29	0.413	17.417
2.96	0.405	17.077
3.98	0.37	15.736
5.51	0.328	13.804
10.67	0.268	11.295
20.23	0.173	7.292
50.31	0.131	5.499
$+\infty$ (open circuit)	0.0956	4.025

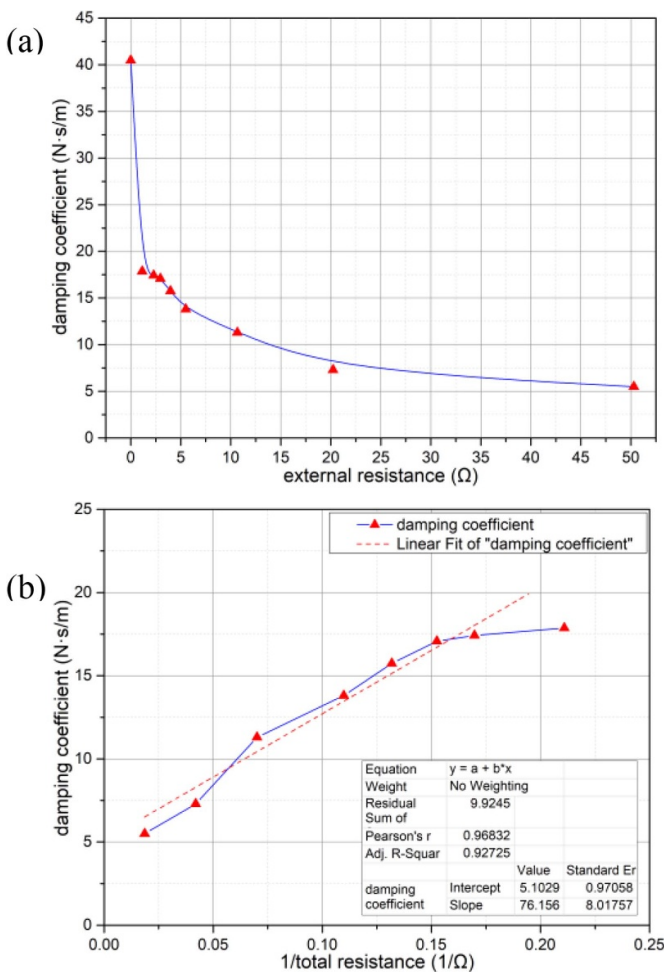


**Figure 13.** Variation of damping coefficient at different resistances: (a) external resistance, (b) reciprocal of total resistance.

The relationship between the damping coefficient and the external resistance follows the reciprocating function of equation (8) as shown in figure 13(a) except at two points where accuracy is not high enough. The slope of the linear fitted line in figure 13(b) between the damping coefficient and the reciprocal of the total resistance is about 76.16 which represents the square of the transduction factor  $K_t$ . The total

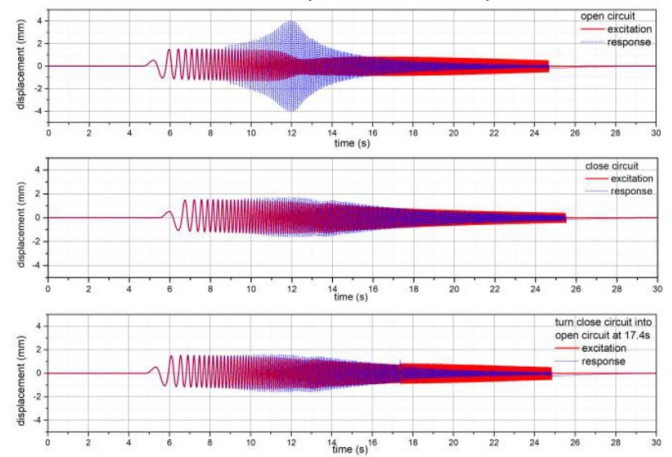


**Figure 14.** Displacement response in time domain with tunable damping. Top: minimum damping with open circuit. Middle: maximum damping with close circuit. Bottom: maximum damping with close circuit in the beginning and changed to minimum damping with open circuit at 17.4 s.

resistance in figure 13(b) is the sum of the internal resistance of the coil ( $3.6 \Omega$ ) and the resistance of the external resistor.

### 3.3. Vibration isolation with tunable damping

The SDOF system response under swept sinusoidal excitation are shown as figure 14. The damping force is tuned to the maximum value at vibration frequency  $\omega < \sqrt{2}\omega_n$  and to the minimum value at vibration frequency  $\omega > \sqrt{2}\omega_n$  in order to minimize the transmissibility of the SDOF system.

In practice, different amount of damping is usually required in different frequency ranges. Higher damping can suppress the resonant response of the SDOF system while lower damping can help save vibration energy at the high-frequency domain. Therefore, the resonant response cannot be suppressed effectively with minimum damping as shown in the upper graph of figure 14. The response amplitudes after crossing the IP at  $\gamma = \sqrt{2}$  is still large with maximum damping as shown in the middle graph of figure 14. The response, however, is reduced in the whole time domain if the damping is at the maximum value and turned into minimum value after crossing the IP at  $\gamma = \sqrt{2}$ . The response in the frequency domain can help to give a clear picture of the tunable damping efficiency of the proposed EMSD.

The measured frequency response functions (FRFs) of the SDOF system are plotted in figure 15. As shown by the blue centerline, significant reduction of transmissibility in the whole frequency domain is obtained when switching the EMSD from maximum damping to minimum damping at the intersection point. The manual switching of electrical resistance in the circuit causes a sudden jump of the damping in the mechanical system and a small fluctuation of the response amplitude in the FRF. Some automatic control methods such as a jitter buffering control algorithm may be used to provide a smoother transition from high to low damping in order to reduce this fluctuation of the response magnitudes of the

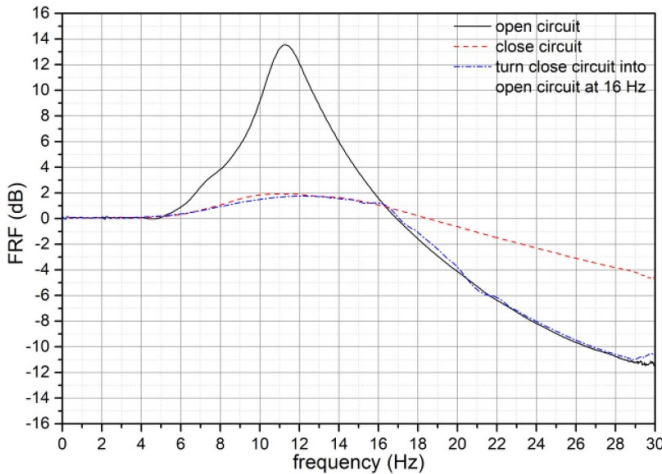


**Figure 15.** Frequency response function (FRF) of the SDOF system with different damping: (1) minimum damping with open circuit, (2) maximum damping with close circuit, (3) switch from maximum damping to minimum damping at the intersection point.

vibrating mass. We choose a simple on-off switch mechanism in the experiment in order to show that the proposed damper can be applied with a simple and low-cost control circuit. Despite its simplicity, the proposed damper can provide desirable damping to the vibrating system excited by sinusoidal or sweep sinusoidal excitation in the experiments. Therefore, the prototype damper at this stage may already be used for damping machine vibrations at constant operating speed as well as during machine startup and shutdown. In the case of random vibration excitation with more rich frequency components, a more sophisticated control system, such as fuzzy logic control, balance logic control or hybrid skyhook-groundhook logic control would be needed in order to produce the desirable damping in real-time. This topic will be our future research work.

#### 4. Conclusions




An electromagnetic shunt damper with tunable damping force is proposed for vibration isolation in this paper. An opposing magnets configuration is proposed to improve the efficiency of EMSD. The proposed EMSD has a significant reduction in size in comparison with other EMSD designs found in the literature. Both simulations and experiments are conducted to verify the improvements of this proposed magnet configuration. As an application example, an EMSD prototype with a six opposing magnets configuration is designed and tested on a SDOF vibration system. The EMSD entails a size reduction of about 46% in comparison with two reference designs found in the literature. Moreover, the damping coefficient of the proposed tunable damper offers a large tunable range with maximum damping coefficient about nine times or 900% of the minimum damping coefficient. The transmissibility of the SDOF system

is minimized in a wide frequency band by varying the damping force in the proposed damper at different vibrating frequencies.

#### Acknowledgments

The authors would like to acknowledge the research funding support from The Hong Kong Polytechnic University (Grant No. 17900184R).

#### ORCID iDs

Ruqi Sun  <https://orcid.org/0000-0002-5926-8971>  
 Waion Wong  <https://orcid.org/0000-0003-3448-8836>  
 Li Cheng  <https://orcid.org/0000-0001-6110-8099>

#### References

- [1] Behrens S., Fleming A J and Moheimani S R 2003 Electromagnetic shunt damping *IEEE/ASME Int. Conf. Adv. Intell. Mechatron.* **2** 1145–50
- [2] Elliott S J and Zilletti M 2014 Scaling of electromagnetic transducers for shunt damping and energy harvesting *J. Sound Vib.* **333** 2185–95
- [3] Zhang X, Niu H and Yan B 2012 A novel multimode negative inductance negative resistance shunted electromagnetic damping and its application on a cantilever plate *J. Sound Vib.* **331** 2257–71
- [4] Niu H, Zhang X, Xie S and Wang P 2009 A new electromagnetic shunt damping treatment and vibration control of beam structures *Smart Mater. Struct.* **18** 045009
- [5] Yan B, Luo Y and Zhang X 2016 Structural multimode vibration absorbing with electromagnetic shunt damping *J. Vib. Control* **22** 1604–17
- [6] Ao W K and Reynolds P 2016 Optimal analysis, design and testing of an electromagnetic damper with resonant shunt circuit for vibration control of a civil structure *Int. Congr. Sound Vib.* **1** 3362–9
- [7] Yan B, Zhang X and Niu H 2012 Design and test of a novel isolator with negative resistance electromagnetic shunt damping *Smart Mater. Struct.* **21** 035003
- [8] Xie L, Li J, Li X, Huang L and Cai S 2018 Damping-tunable energy-harvesting vehicle damper with multiple controlled generators: design, modeling and experiments *Mech. Syst. Signal Process.* **99** 859–72
- [9] Stabile A, Aglietti G S, Richardson G and Smet G 2017 Design and verification of a negative resistance electromagnetic shunt damper for spacecraft micro-vibration *J. Sound Vib.* **386** 38–49
- [10] Zuo L, Scully B, Shestani J and Zhou Y 2010 Design and characterization of an electromagnetic energy harvester for vehicle suspensions *Smart Mater. Struct.* **19** 045003
- [11] Kremer D and Liu K 2014 A nonlinear energy sink with an energy harvester: transient responses *J. Sound Vib.* **333** 4859–80
- [12] Sun R and Wong W 2019 Vibration control with a tunable self-sensing electromagnetic shunt damper *23rd Int. Conf. on Mechatronics Technology (ICMT) IEEE*
- [13] Clarence W C 2007 *Vibration Damping, Control, and Design* (Boca Raton, London and New York: Taylor & Francis Group)